Hyper-reduced arc-length algorithm for stability analysis in elastoplasticity

H. Launay, Jacques Besson, David Ryckelynck, François Willot

Hyper-reduced arc-length algorithm for stability analysis in elastoplasticity

H. Launay[a], J. Besson[a], D. Ryckelynck[a,*], F. Willot[a,b]

[a] *MINES ParisTech, PSL research university, Centre des Matériaux, CNRS UMR 7633, 91003 Evry, France*

[b] *Centre de Morphologie Mathématiques, 77300 Fontainebleau, France*

Ref: International Journal of Solids and Structures 208–209 pp. 167–180 (2021).

Abstract

In this article an "hyper-reduced" scheme for the Crisfield's algorithm (Crisfield, 1981) applied to buckling simulations and plastic instabilities is presented. The two linear systems and the ellipse equation entering the algorithm are projected on a reduced space and solved in a reduced integration domain, resulting in a system of "hyper-reduced" equations. Use is made of the Gappy proper orthogonal decomposition to recover stresses outside the reduced integration domain. Various methods are proposed to construct a reduced bases, making use of simulation data obtained with standard finite element method and a stress-based error criterion for the hyper reduced calculations is proposed. A "greedy" algorithm coupled with this error criterion is used to generate intelligently full standard finite element simulations and enrich the reduced base, demonstrating the adequacy of the error criterion. Finally, numerical results pertaining to elastoplastic structures undergoing finite strains, with emphasis on buckling and limit load predictions are presented. A parametric study on the geometry of the structure is carried out in order to determine the domain of validity of the proposed hyper-reduced modeling approach.

Keywords: Model order reduction; Hyper-reduction; Reduced integration domain; Crisfield algorithm; POD; Plastic instability; Buckling; Limit load

*Corresponding author

URL: david.ryckelynck@mines-paristech.fr (D. Ryckelynck)

1. Introduction

Micromechanical computations are often coupled with parametric studies to probe the mechanical behavior of structures undergoing plastic instabilities, and determine the effect of shape and geometry, material laws and mechanical loadings. The prediction of the limit load of structures [1] is an important aim of many of these methods. However efficient the approaches might be, the scope of a parametric study, its extent in the space of parameters, is constrained by the numerical method it employs – and ultimately by how fast numerical computations can be carried out. Parametric studies become especially challenging when dealing with unstable elasto-plastic problems, modeled as sets of partial differential equations, each of which must be solved numerically. The computational complexity of the resulting method is driven by the size of the approximation space used to represent the solution of the problem. As an example, the size of the "full-order model" (FOM), used in the finite element method, is proportional to the number of discrete unknowns, and is generally quite high. To overcome this limitation, methods employing reduced bases have been developed since the 1970s [2] and have seen wide applications in a variety of mechanical problems [3, 4]. As a principle, the reduced base defines the approximation space on which solutions are sought for. The corresponding reduced-order model (ROM) is obtained by projecting the full-order model on the reduced base. Techniques for deriving a model-order reduction method based on projections have been developed for a long time [5]. Nevertheless, recent publications show interesting hybrid approaches combining deep-learning and reduced-modeling for partial differential equations (PDEs). In [6], for instance, a solution of PDEs obtained by neural networks is proposed. In the context of non-parametric modeling, other authors [7, 8] make use of convolutional neural networks to tailor hyper-reduced order models, which are useful when the number of parameters is large, typically more than 100.

Hyper-reduction methods [9], which, commonly, make use of the Newton-Raphson scheme, offer computational speed-up for stable elastoplastic simulations [10, 11]. The Newton-Raphson algorithm is, however, not robust enough when dealing with unstable elastoplastic problems, where critical loads or buckling must be accounted for. The Newton Raphson algorithm may diverge, for instance, due to snap-through or a snap-back equilibrium states [12]. The "asymptotic numerical method" [13] or the "arc-length method" [14, 15, 16] have been developed to treat these problems. The arc-length method is a general technique for structural analysis originally developed by Riks [17]. Later, other authors [18, 19] have developed refined schemes. Arc-length algorithms are especially useful to treat highly-nonlinear problems such as delamination or fracture [20, 21].

The present work is devoted to the estimation of the critical load of ductile pipelines undergoing rupture [22, 23]. The critical loads of structures may be estimated using charts at virtually no cost [24]. This approach provides results instantaneously. Yet, it is valid for

specific geometries only, and overestimate the effect of geometry in many cases. To predict accurately the critical load of pipelines, the size and shape of the structures should be taken into account. In the present article, a hyper-reduction method based on Crisfield's algorithm is proposed as a way to limit the computational cost of solving an implicit nonlinear balanced equations, while offering accurate mechanical predictions.

Many reduced-order models have been developed to deal with such nonlinear problems. In interpolation methods, the nonlinear terms of interest are estimated by interpolation at a few spatial locations [25]. In particular, in the discrete empirical interpolation method (DEIM) [26], the set of interpolation points is obtained using a proper orthogonal decomposition (POD) base. In cubature methods [27, 28, 29, 30], spatial integrals involved in the weak formulation are estimated using a few unassembled elemental contributions. The elements of interest and weight coefficients are determined using an optimization process. The third types of methods are boundary value problems restricted to a reduced integration domain (RID) [31]. The RID usually involve elements connected to interpolation points computed by the DEIM algorithm, and can be obtained by considering several POD reduced bases. This last approach has been successfully applied to elastoplastic [32] and contact problems [11] and is followed here. For simplicity, the boundary value problem restricted to a reduced integration domain is denoted "HR" hereafter.

In the present work, the hyper-reduction method is extended to the Crisfield's algorithm consists in coupling the usual hyper-reduced residual to a reduced ellipse equation. With Crisfield's method two linear systems are solved resulting in two solutions. The global solution is a linear combination of these two vectors, under a constraint prescribed by an ellipse. In this paper, various reduced order bases (ROB) constructions are considered by taking into account the contributions to the global solution. In order to choose relevant snapshots, a greedy sampling algorithm coupled with an error indicator is proposed. This strategy ensures the robustness of the reduced order model with respect to variations of the model parameters. In order to undertake fast parametric studies, a reduced model is developed by projecting the mechanical equations on a reduced order base (ROB) with a hyper-reduced method.

Section 2 presents the notation that will be used. The Crisfield algorithm is described in section 3 whereas section 4 is dedicated to the classical hyper-reduced method. Section 5 details the hyper-reduced arc-length algorithm. Section 6 shows various results with this method. Finally in section 7 the speed up of this method is discussed.

2. Notations

In this article, scalar values are denoted by lowercase roman letters, vectors by bold lowercases, and matrices by uppercase, bold letters, e.g. a, $\mathbf{a}$ and $\mathbf{A}$ respectively. The

notation $\mathbf{A}[L_1, L_2]$ designates the submatrix of $\mathbf{A}$ formed by the subset L_1 of the rows of $\mathbf{A}$ and the subset L_2 of the columns of $\mathbf{A}$. We use the Python-notation $\mathbf{A}[L_1, :]$ for the submatrix formed by a subset L_1 of the rows of $\mathbf{A}$. Second-order tensors are denoted by underlined capitals (e.g. $\underset{\sim}{A}$) whereas fourth-order tensors are underlined twice ($\underset{\approx}{C}$). Double-dots (:) designate a double contraction over the last two and first two indices of the left and right tensors, respectively. As such $\underset{\sim}{A} : \underset{\sim}{B}$ is the scalar $\sum_{ij} \; A_{ij} \; B_{ij}$ whereas $\underset{\approx}{C} : \underset{\sim}{B}$ is the second-order tensor $\sum_{kl} \; C_{ijkl} \; B_{kl}$.

The Euclidian norm (or 2-norm) is denoted by the symbols $||.||_2$. It is defined by $||\mathbf{u}||_2 = (\mathbf{u}^T \cdot \mathbf{u})^{1/2} = (\sum_i u_i^2)^{1/2}$ where the superscript ^{T} designates a matrix transpose. The 2-norm of matrices is given by the spectral norm $||\mathbf{A}||_2 = \sigma_{max}(\mathbf{A})$, where $\sigma_{max}(\mathbf{A})$ denotes the largest singular value of $\mathbf{A}$.

3. Crisfield's algorithm for unstable finite element problems

The present section is devoted to Crisfield's algorithm. This algorithm, developed to achieve convergence in unstable problems, is described hereafter. In the context of the finite element (FE) model [33], the shape functions of the FE base are denoted by $(\phi_j)_{j=1}^n$ with n the number of discretization nodes. It is convenient to introduce the functions $\boldsymbol{\phi}_i = \phi_j \mathbf{e}_k$ where $i = (j-1) \times d + k$, $n = 1, ..., n$, $k = 1, ..., d$, d is the dimension of the problem and $\mathbf{e}_k$ refer to the canonical vectors of a Cartesian coordinate system. The decomposition of the displacement with the shape functions $(\boldsymbol{\phi}_j)_{j=1}^{\mathcal{N}}$ reads:

$$\boldsymbol{v}(\mathbf{x}) = \boldsymbol{v}_0(\mathbf{x}) + \sum_{i=1}^{\mathcal{N}} \boldsymbol{\phi}_i(\mathbf{x}) u_i, \qquad \forall \mathbf{x} \in \Omega, \tag{1}$$

where $\mathcal{N} = n \times d$ is the number of degrees of freedom (DOF) of the structure, $\boldsymbol{v}_0$ is a given displacement field that fulfills the Dirichlet boundary conditions, $\boldsymbol{v}$ is the approximate finite element solution and $\mathbf{u} = (u_i)_{i=1}^{\mathcal{N}}$ the vector of the related degrees of freedom. The Cauchy stress that fulfills the constitutive equations is denoted by $\underset{\sim}{\sigma}(\mathbf{u})$. Denote $\mathbf{f}^{int} \in \mathbb{R}^{\mathcal{N}}$ a vector of generalized internal forces which depends on $\mathbf{u}$ such that:

$$f_i^{int}(\mathbf{u}) = \int_\Omega \frac{1}{2} \left(\underset{\sim}{\nabla} \boldsymbol{\phi}_i + \underset{\sim}{\nabla}^T \boldsymbol{\phi}_i \right) : \underset{\sim}{\sigma}(\mathbf{u}) \, d\Omega, \qquad i = 1, \dots \mathcal{N}, \tag{2}$$

where Ω is the current configuration. The focus of the present work is now limited to implicit solutions of finite element balance equations, where use is made of an arc-length algorithm [34]. Because of instabilities or plasticity, the target loading may be out of reach.

Accordingly, the magnitude of the loading, denoted $\lambda \in \mathbb{R}$, should be determined as well as the displacement field. The residual of the FE balance equation reads:

$$\mathbf{r}(\mathbf{u}, \lambda) = \mathbf{f}^{int}(\mathbf{u}) - \lambda\, \mathbf{f}^{ext}, \tag{3}$$

where $\mathbf{f}^{ext} \in \mathbb{R}^{\mathcal{N}}$ denotes the vector of general external loading. The residual is assumed to be null in the initial configuration:

$$\mathbf{f}^{int}(\mathbf{u}_0) - \lambda_0\, \mathbf{f}^{ext} = 0. \tag{4}$$

The couple of variables ($\Delta\mathbf{u}$, $\Delta\lambda$) is determined so as to satisfy a null residual in the current configuration:

$$\mathbf{r}(\mathbf{u}_0 + \Delta\mathbf{u}, \lambda_0 + \Delta\lambda) = 0. \tag{5}$$

As a consequence of the above (5), point ($\mathbf{u}_0$+$\Delta\mathbf{u}$, λ_0+$\Delta\lambda$) belongs to the equilibrium path. Assume that the residual is not zero at point ($\mathbf{u}_0$+$\Delta\mathbf{u}$, λ_0+$\Delta\lambda$), i.e. $\mathbf{r}(\mathbf{u}_0$+$\Delta\mathbf{u}, \lambda_0$+$\Delta\lambda) \neq 0$. A solution at a nearby point ($\mathbf{u}_0 + \Delta\mathbf{u} + \delta\mathbf{u}$, $\lambda_0 + \Delta\lambda + \delta\lambda$) is sought for. A Taylor expansion provides the expression:

$$\mathbf{r}(\mathbf{u}_0 + \Delta\mathbf{u} + \delta\mathbf{u}, \lambda_0 + \Delta\lambda + \delta\lambda) \approx \mathbf{r}(\mathbf{u}_0 + \Delta\mathbf{u}, \lambda_0 + \Delta\lambda) + \mathbf{K} \cdot \delta\mathbf{u} - \delta\lambda\, \mathbf{f}^{ext} \tag{6}$$

where $\mathbf{K} = \partial\mathbf{f}^{int}/\partial\mathbf{u}|_{\mathbf{u}=\mathbf{u}_0+\Delta\mathbf{u}}$. The linearized balance equation accordingly reads:

$$\mathbf{K} \cdot \delta\mathbf{u} - \delta\lambda\, \mathbf{f}^{ext} = -\mathbf{r}(\mathbf{u}_0 + \Delta\mathbf{u}, \lambda_0 + \Delta\lambda) \tag{7}$$

The variables $\delta\mathbf{u}$ and $\delta\lambda$ being the unknowns, equation (7) does not yield a unique solution. Indeed the problem is constrained by $\mathcal{N}$ scalar equations depending on $\mathcal{N}+1$ unknowns, including $\delta\lambda$. The problem ought to be supplemented by an additional "arc-length equation" [15] which describes an ellipse in the space of displacement and loading parameters. The latter reads:

$$(\Delta\mathbf{u} + \delta\mathbf{u})^T \cdot (\Delta\mathbf{u} + \delta\mathbf{u}) + \beta^2(\Delta\lambda + \delta\lambda)^2(\mathbf{f}^{ext\ T} \cdot \mathbf{f}^{ext}) = \Delta\ell^2, \tag{8}$$

$\Delta\ell$ represents the radius of the circle on which the solution $(\delta\mathbf{u}, \delta\lambda)$ must be found. This is a user defined parameter relative to the size of the increment. In the above, β is also a user defined parameter which monitors the shape of the ellipse. As an example β=1 leads to a circle hence the name "arc-length method". Figure1 depicts the arc-length algorithm with the choice $\beta = 1$.

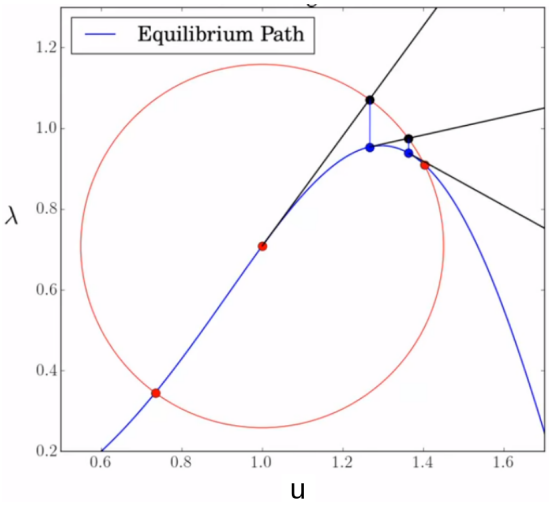

Figure 1: Arc-length method.

Each blue point represents the solution of an iteration until it converges at the red dot on the right. Following [18], equation (7) can be written:

$$\mathbf{K} \cdot \delta\mathbf{u} = \delta\lambda\, \mathbf{f}^{ext} - \mathbf{r}(\mathbf{u}_0 + \Delta\mathbf{u}, \lambda_0 + \Delta\lambda). \tag{9}$$

which is solved in terms of two solutions $\delta\mathbf{u}_b$ and $\delta\mathbf{u}_t$ for the linearised balance equation:

$$\begin{cases} \mathbf{K}.\delta\mathbf{u}_t = \mathbf{f}^{ext} \\ \mathbf{K}.\delta\mathbf{u}_b = -\mathbf{r}(\mathbf{u}_0 + \Delta\mathbf{u}, \lambda_0 + \Delta\lambda) \\ \delta\mathbf{u} = \delta\mathbf{u}_b + \delta\lambda\, \delta\mathbf{u}_t. \end{cases} \tag{10}$$

As shown by the above, the Crisfield algorithm involves two balance equations of the finite element model. Equation (10a) relates to the target loading whereas equation (10b), similar to the linear step involved in the Newton-Raphson algorithm, relates to the residual stresses in the structure. The projection-based model-order reduction aimes to reduce the computational complexity of these two balance equation related to the two primal variables $\delta\mathbf{u}_b$ and $\delta\mathbf{u}_t$. According to (10c), equation (8) may be rewritten as:

$$\begin{aligned} &(\Delta\mathbf{u} + \delta\mathbf{u})^T \cdot (\Delta\mathbf{u} + \delta\mathbf{u}) + \beta^2(\Delta\lambda + \delta\lambda)^2(\mathbf{f}^{ext\ T} \cdot \mathbf{f}^{ext}) = \Delta\ell^2 \\ &\Longleftrightarrow \\ &\alpha_1\delta\lambda^2 + \alpha_2\delta\lambda + \alpha_3 = 0, \end{aligned} \tag{11}$$

where:

$$\begin{aligned}
\alpha_1 &= \delta\mathbf{u}_t^T \cdot \delta\mathbf{u}_t + \beta^2 \mathbf{f}^{ext\ T} \cdot \mathbf{f}^{ext} \\
\alpha_2 &= 2(\Delta\mathbf{u} + \delta\mathbf{u}_b)^T \cdot \delta\mathbf{u}_t + \beta^2 \Delta\lambda \mathbf{f}^{ext\ T} \cdot \mathbf{f}^{ext} \\
\alpha_3 &= (\Delta\mathbf{u} + \delta\mathbf{u}_b)^T \cdot (\Delta\mathbf{u} + \delta\mathbf{u}_b) + \beta^2 \Delta\lambda \mathbf{f}^{ext\ T} \cdot \mathbf{f}^{ext} - \Delta\ell^2
\end{aligned} \tag{12}$$

As expected for ellipses, equation (11) admits two solutions, denoted $\delta\lambda_1$ and $\delta\lambda_2$ Following on the "dot-product rule" introduced in [35], the solution in the equilibrium path maximizes the quantity:

$$D^{(i)} = (\Delta\mathbf{u} + \delta\mathbf{u}^{(i)})^T \cdot \Delta\mathbf{u} + \beta^2 \Delta\lambda(\Delta\lambda + \delta\lambda^{(i)}) \left(\mathbf{f}^{ext}\right)^T \cdot \mathbf{f}^{ext}, \qquad i = 1, 2, \tag{13}$$

which ensures that the selected solution is the closest to previously-computed solutions. This rule allows one to deform the structure while preventing elastic unloading in most of the cases. Once $\delta\mathbf{u}$ and $\delta\lambda$ is obtained, the incremental displacement $\Delta\mathbf{u}$ and incremental loading parameter $\Delta\lambda$ are updated until the norm of the residual is smaller than a specified threshold. Furthermore, when convergence is found to be slow, a novel incremental solution is sought for the same problem with a lower $\Delta\ell$ parameter.

It is emphasized that equation (8) mixes displacement and force, and therefore the variables α_i have no clear physical meaning. To overcome this problem, the parameter β may be set to zero, in which case $\Delta\ell$ denotes the distance between the two possible values of $\Delta\mathbf{u}$. In the rest of the study, the value of β is assumed to be zero.

4. Hyper-reduction method

This section is devoted to the usual hyper-reduced method using the Newton-Raphson algorithm, in this case the balance equation takes the form of equation (9), with $\delta\lambda = 0$ and $\Delta\lambda$ being the loading increment which is a constant in this case. Therefore only the iterative displacement vector $\delta\mathbf{u}$ is unknown.The following equation is obtained :

$$\mathbf{K} \cdot \delta\mathbf{u} = -\mathbf{r}(\mathbf{u}_0 + \Delta\mathbf{u}, \lambda_0 + \Delta\lambda). \tag{14}$$

As previously stated, this approach belongs to projection-based reduction methods, and aims to reduce the number of DOFs by projecting the balance equation on a smaller approximation space. Here, hyper-reduction is applied in the framework of a posteriori model reduction methods and unsupervised machine learning methods. In these methods, the computational task is divided in two phases, namely an "offline" and "online phase". In the offline phase, simulation data are generated by the solution of the high-fidelity equations, possibly for various parameter values in a training set $\mathcal{D}_{train}$. These simulation data

are called training data and are required to train reduced bases and a reduced integration domain (RID). In the online phase, the HR model is used to predict the displacements and other quantities of interest resulting from parameters values which do not belong to the training set. Offline phases are time-consuming as they require solutions of the FOM for different sampling points in the parameter space. Nevertheless, they allow for low-cost online simulations afterwards, provided the hyper-reduced order model (HROM) can be used. Projection-based model order reduction methods may be combined with robust machine-learning methods. Hybrid approaches [7, 8] have been proposed which make use of physical equations and data science techniques. These methods are particularly efficient ways to take advantage of simulation data. In this context, and in the context of model-order reduction, it is useful to save these data in memory storage systems.

The HR method [10] uses a projection on a reduced base to reduce the number of DOFs, but it also uses the fact that solving the equations on a RID is sufficient to find the reduced DOFs with less computational complexity than using the full domain. This particularity improves the computational time savings, especially for nonlinearities that cannot be precomputed offline. Indeed, the RID, built during the offline part, reduces the cost of the projections to get the reduced non-constant stiffness matrix from the Jacobian matrix. The reduced base for displacement approximation is obtained via the singular value decomposition (SVD). The reader is referred to [2] for a discussion of the connections between proper orthogonal decomposition methods (POD) and SVD. The SVD is a common numerical tool in machine learning and especially useful when computing principal components. According to the Young Eckart theorem [36], it provides, in particular, the optimal low-rank approximation of the simulation data generated during the offline phase. In the following details on the methodology of the hyper-reduction method are given.

Let us denote $\mathcal{N}_\mathcal{S}$ the number of displacement fields available at the end of the offline phase. The nodal value of these finite element fields are stored in a snapshot matrix $\mathbf{Q} \in \mathbb{R}^{\mathcal{N} \times \mathcal{N}_\mathcal{S}}$. For each parameter in the training set $\mathcal{D}_{train}$, and at each time increment the approximation of the balance equation is satisfied and the displacement $\mathbf{u}$ computed by the parametric finite element model is saved as a column of $\mathbf{Q}$, such that $\exists\, j \in \{1, \ldots, \mathcal{N}_\mathcal{S}\}$ with $\mathbf{Q}[:, j] = \mathbf{u}$. Then, a truncated singular value decomposition is applied in order to extract the reduced base $\mathbf{V}$ according to the following optimal low-rank approximation:

$$\mathbf{Q} = \mathbf{V} \cdot \mathbf{\Sigma} \cdot \mathbf{W}^T + \mathbf{R}, \quad \mathbf{V}^T \cdot \mathbf{V} = \mathbf{I}_N, \quad \mathbf{W}^T \cdot \mathbf{W} = \mathbf{I}_N, \quad \mathbf{V}^T \cdot \mathbf{R} = 0, \quad \frac{\|\mathbf{R}\|_2^2}{\|\mathbf{Q}\|_2^2} < \epsilon_{tol}, \tag{15}$$

where $\mathbf{I}_N$ is the identity matrix and belongs to $\mathbb{R}^{N \times N}$, $\mathbf{R}$ belongs to $\mathbb{R}^{\mathcal{N} \times \mathcal{N}_\mathcal{S}}$ and ϵ_{tol} is an error-criterion. The matrices $\mathbf{V} \in \mathbb{R}^{\mathcal{N} \times N}$ and $\mathbf{W} \in \mathbb{R}^{\mathcal{N}_\mathcal{S} \times N}$ are orthogonal matrices and $\mathbf{\Sigma} \in \mathbb{R}^{N \times N}$ is a diagonal matrix which contains the highest singular values σ_j in descending order (i.e. $\sigma_j \geq \sigma_{j+1}$). In the present case, simulation data are related to a finite element

model so that each column of $\mathbf{V}$ is the nodal values of an empirical mode $\boldsymbol{\psi}_k$ where:

$$\boldsymbol{\psi}_k(\mathbf{x}) = \sum_{i=1}^{\mathcal{N}} \boldsymbol{\phi}_i(\mathbf{x})\, V_{ik}, \qquad k = 1, \dots N, \qquad \mathbf{x} \in \Omega. \tag{16}$$

The importance of an empirical mode is quantified by the corresponding value σ_j. The truncation of the SVD, and the number of empirical modes stored in $\mathbf{V}$, is monitored by the error-criterion ϵ_{tol}. Ideally, the reduced base $\mathbf{V}$ contains a few vectors and allows one to approximate the space spanned by the snapshots.

The above reduced-base construction may be applied to any finite element variables, either defined at the nodes of the mesh, or at the Gauss points inside elements. A reduced-base is most often generated for both displacement variables and stresses separately (details about the stress field involved in the computation of $\mathbf{f}_{int}$ will be given in Section 6.1). In the present work, the stress-related reduced base is denoted by $\mathbf{V}^\sigma$.

Following on the Gappy POD [37], any vector $\mathbf{u}$ which belongs to the column space *colspan*$(\mathbf{V})$ of $\mathbf{V}$ may be recovered by using few entries $\mathbf{u}[\mathcal{F}]$ of $\mathbf{u}$, if $\mathbf{V}[\mathcal{F},:]$ is a full column rank matrix. Such recovery procedure takes the form:

$$\mathbf{u} \in \mathit{colspan}(\mathbf{V}), \qquad \mathbf{u} = \mathbf{V} \cdot \left(\mathbf{V}[\mathcal{F},:]^T \cdot \mathbf{V}[\mathcal{F},:]\right)^{-1} \cdot \mathbf{V}[\mathcal{F},:]^T \cdot \mathbf{u}[\mathcal{F}]. \tag{17}$$

In the case $\mathcal{F} = \mathcal{P}$, where $\mathcal{P}$ denotes the set of interpolation points for columns of $\mathbf{V}$ obtained by the discrete empirical interpolation method (DEIM) [26], the matrix $\mathbf{V}[\mathcal{P},:]$ is square invertible and the recovery procedure simplifies as:

$$\mathbf{u} \in \mathit{colspan}(\mathbf{V}) \quad \mathbf{u} = \mathbf{V} \cdot \mathbf{V}[\mathcal{P},:]^{-1} \cdot \mathbf{u}[\mathcal{P}]. \tag{18}$$

Moreover, if $\mathcal{P} \subset \mathcal{F}$, then $\mathbf{V}[\mathcal{F},:]$ is full-column rank.

A heuristic rule is followed to construct the RID: the extent of the RID must enable the recovery of the finite element displacement fields and the finite element stresses when they both belong to *colspan*$(\mathbf{V})$ and *colspan*$(\mathbf{V}^\sigma)$ respectively. Notice that the recovery of the stress enables the estimation of $\mathbf{f}_{int}$ and of the residual, without using an interpolation scheme for $\mathbf{f}_{int}$. The set of interpolation points related to $\mathbf{V}^\sigma$ is denoted by $\mathcal{P}^\sigma$. Hence, $\mathcal{F}$ is generated such that $\mathcal{P} \cup \mathcal{P}^\sigma \subset \mathcal{F}$ which allows one to recover the stress and the displacement, making use of the Gappy POD. In many practical situations, $\mathcal{F}$ also includes the degrees of freedom of a zone of interest.

The RID, denoted by $\Omega_A \subset \Omega$, is assumed to be the support of the finite element shape functions $\boldsymbol{\phi}_i$ $(i \in \mathcal{F})$:

$$\Omega_A = \cup_{i \in \mathcal{F}} \mathrm{sup}(\boldsymbol{\phi}_i). \tag{19}$$

Denote $\Omega_B = \Omega \backslash \Omega_A$ the complementary set of Ω_A and $\Gamma^I = \overline{\Omega_A} \cap \overline{\Omega_B}$ the interface common to Ω_A and Ω_B. The following property holds:

$$\mathcal{F} = \left\{ i \in \{1, ..., \mathcal{N}\} \mid \int_{\Omega_B} \boldsymbol{\phi}_i^T \,.\, \boldsymbol{\phi}_i \; d\Omega = 0 \right\} \tag{20}$$

Let us now introduce $\mathcal{I}$, the set of degrees of freedom indices related to the interface Γ^I:

$$\mathcal{I} = \left\{ i \in \{1, ..., \mathcal{N}\} \mid \int_{\Gamma^I} \boldsymbol{\phi}_i^T \,.\, \boldsymbol{\phi}_i \; d\Gamma \neq 0 \right\} \tag{21}$$

The matrix $\mathbf{K}$ entering equation is sparse. The assumption is made that non zero-entries in $\mathbf{K}[\mathcal{F}, :]$ are only in the submatrix $\mathbf{K}[\mathcal{F}, \mathcal{F} \cup \mathcal{I}]$ and these entries can be computed by using solely the reduced mesh that covers Ω_A. This assumption is too strong in case of contact problems as shown in [11]. For the sake of simplicity, the focus of this article is, hereafter limited to contactless problems. The reader is refered to [11] for more details on hyper-reduction methods associated to contact problems.

The HR method is based on the equation (17) in the case that the variable $\mathbf{u}$ must be computed via a balance equation. In the following the balance equation (14) is considered. The hyper-reduced coordinates vector $\delta\boldsymbol{\gamma}$ is introduced such that $\delta\mathbf{u} = \mathbf{V} \cdot \delta\boldsymbol{\gamma}$. The values contained in this vector are weights for the modes of the reduced-base vector $\mathbf{V}$. The obtained hyper-reduced solution is a linear combination of the modes of the reduced base. The hyper-reduced problem consists in finding $\delta\boldsymbol{\gamma} \in \mathbb{R}^N$ such that $\delta\mathbf{u} = \mathbf{V}\, \delta\boldsymbol{\gamma}$ and:

$$\mathbf{V}[\mathcal{F}, :]^T \cdot \mathbf{K}[\mathcal{F}, \mathcal{F} \cup \mathcal{I}] \cdot \mathbf{V}[\mathcal{F} \cup \mathcal{I}, :] \cdot \delta\boldsymbol{\gamma} = -\mathbf{V}[\mathcal{F}, :]^T \cdot \mathbf{r}(\mathbf{u} + \Delta\mathbf{u}, \lambda_0)[\mathcal{F}]. \tag{22}$$

The hyper-reduced matrix and the hyper-reduced residual are given by:

$$\mathbf{K}^{HR} = \mathbf{V}[\mathcal{F}, :]^T \cdot \mathbf{K}[\mathcal{F}, \mathcal{F} \cup \mathcal{I}] \cdot \mathbf{V}[\mathcal{F} \cup \mathcal{I}, :], \tag{23a}$$

$$\mathbf{r}^{HR}(\mathbf{u}_0 + \Delta\mathbf{u}, \lambda) = \mathbf{V}[\mathcal{F}, :]^T \cdot \mathbf{r}(\mathbf{u}_0 + \Delta\mathbf{u}, \lambda)[\mathcal{F}]. \tag{23b}$$

Let us emphasize the following remarks:

- Formally, if $\mathbf{r} = -\delta\mathbf{u}$ and $\mathbf{K}$ is the identity matrix, then $\mathcal{I} = \emptyset$ and the HR balance equation is equivalent to the recovery equation of the Gappy POD.
- The matrix $\mathbf{V}[\mathcal{F}, :]^T$ in Equation (22) is related to the test functions $\boldsymbol{\psi}_k^Z = \sum_{i \in \mathcal{F}} \boldsymbol{\phi}_i V_{ik}$ for $k = 1, \dots N$. When introduced as a weak form of the hyper-reduced balance equations, it is emphasized that the test functions have a similar form that obtained for Dirichlet boundary conditions on the interface Γ^I. The reader is referred to [31] for more details about the boundary conditions used for hyper-reduced problems.

5. Hyper-reduced arc-length algorithm

The extension of the HR method to the Crisfield's algorithm is straightforward when choosing the same reduced base and the same RID for the two balance equations involved in the system of equations (10). This reduced base must be accurate enough for the approximation of both $\delta\mathbf{u}_t$ and $\delta\mathbf{u}_b$. Consider now the hyper-reduced external forces vector:

$$\mathbf{f}^{ext}_{HR} = \mathbf{V}[\mathcal{F},:]^T \cdot \mathbf{f}^{ext}[\mathcal{F}]. \tag{24}$$

In the hyper-reduced arc-length problem, $\delta\boldsymbol{\gamma}_t \in \mathbb{R}^N$, $\delta\boldsymbol{\gamma}_b \in \mathbb{R}^N$ and $\delta\lambda$ are sought for such that $\delta\mathbf{u}_t = \mathbf{V}\cdot\delta\boldsymbol{\gamma}_t$, $\delta\mathbf{u}_b = \mathbf{V}\cdot\delta\boldsymbol{\gamma}_b$ and:

$$\begin{cases} \mathbf{K}^{HR}\cdot\delta\boldsymbol{\gamma}_t = \mathbf{f}^{ext}_{HR} \\ \mathbf{K}^{HR}\cdot\delta\boldsymbol{\gamma}_b = -\mathbf{r}^{HR}(\mathbf{u}_0 + \mathbf{V}\Delta\boldsymbol{\gamma}, \lambda_0 + \Delta\lambda) \\ \delta\boldsymbol{\gamma} = \delta\boldsymbol{\gamma}_b + \delta\lambda\,\delta\boldsymbol{\gamma}_t \\ (\Delta\boldsymbol{\gamma}+\delta\boldsymbol{\gamma})^T\cdot(\Delta\boldsymbol{\gamma}+\delta\boldsymbol{\gamma}) + \beta^2(\Delta\lambda+\delta\lambda)^2(\mathbf{f}^{ext\ T}\cdot\mathbf{f}^{ext}) = \Delta\ell^2, \end{cases} \tag{25}$$

where $\Delta\boldsymbol{\gamma}$ has been updated to $\Delta\boldsymbol{\gamma}+\delta\boldsymbol{\gamma}$, assuming the norm of $\mathbf{r}^{HR}(\mathbf{u}_0+\mathbf{V}\cdot\Delta\boldsymbol{\gamma}, \lambda_0+\Delta\lambda)$ is lower than a given tolerance. Here equation (25d) defines a reduced form of equation (8)

Property: If $\Delta\mathbf{u} = \mathbf{V}\cdot\Delta\gamma$, $\delta\mathbf{u} = \mathbf{V}\cdot\delta\gamma$ and $\mathbf{V}^T\cdot\mathbf{V} = \mathbf{I}$, then the solutions of equation (25d) and that of (8) are identical.

The above is a consequence of (8), which entails:

$$(\Delta\boldsymbol{\gamma}+\delta\boldsymbol{\gamma})^T\cdot\mathbf{V}^T\cdot\mathbf{V}\cdot(\Delta\boldsymbol{\gamma}+\delta\boldsymbol{\gamma}) + \beta^2(\Delta\lambda+\delta\lambda)^2(\mathbf{f}^{ext\ T}\cdot\mathbf{f}^{ext}) = \Delta\ell^2.$$

and reduce to the equation (25d) after replacing $\mathbf{V}^T\cdot\mathbf{V}$ by $\mathbf{I}$.

Property: If $\delta\mathbf{u}_t = \mathbf{V}\cdot\delta\gamma_t$, $\delta\mathbf{u}_b = \mathbf{V}\cdot\delta\gamma_b$, λ are the exact solutions of equations (10) and (8), then γ_t, γ_b and λ are the solutions of the hyper-reduced arc-length equations (25).

Proof: If $\delta\mathbf{u}_t = \mathbf{V}\cdot\delta\gamma_t$, $\delta\mathbf{u}_b = \mathbf{V}\cdot\delta\gamma_b$ and λ are the exact solutions of the original equations, then:

$$\begin{aligned}
\exists\Delta\gamma: \quad \Delta\mathbf{u} &= \mathbf{V}.\Delta\gamma, && \text{(26a)}\\
\mathbf{K}[\mathcal{F},\mathcal{F}\cup\mathcal{I}].\mathbf{V}[\mathcal{F}\cup\mathcal{I},:]\delta\gamma_t &= \mathbf{f}^{ext}[\mathcal{F}], && \text{(26b)}\\
\mathbf{K}[\mathcal{F},\mathcal{F}\cup\mathcal{I}]\mathbf{V}[\mathcal{F}\cup\mathcal{I},:]\delta\gamma_b &= -\mathbf{r}(\mathbf{u}+\Delta\mathbf{u}, \lambda_0+\Delta\lambda)[\mathcal{F}], && \text{(26c)}\\
\delta\boldsymbol{\gamma} &= \delta\gamma_b + \delta\lambda\,\delta\gamma_t, && \text{(26d)}\\
(\Delta\boldsymbol{\gamma}+\delta\boldsymbol{\gamma})^T\cdot(\Delta\boldsymbol{\gamma}+\delta\boldsymbol{\gamma}) &= \Delta\ell^2 - \beta^2(\Delta\lambda+\delta\lambda)^2(\mathbf{f}^{ext\ T}\cdot\mathbf{f}^{ext}). && \text{(26e)}
\end{aligned}$$

According to the above, the hyper-reduced arc-length equations (25) are fulfilled by $\delta\gamma_t$, $\delta\gamma_b$ and $\delta\lambda$.

Let us now investigate the computational complexity of the proposed method. The later does not scale proportionally to $\mathcal{N}$, as a finite element model would do. Instead, $\mathbf{K}^{HR}$ being a full matrix, the solution of hyper-reduced linear systems has a computational complexity proportional to N^3. So in order to achieve a good speed up of the method it is necessary to have $N^3 \ll \mathcal{N}$. Moreover, for a given residual $\mathbf{r}$, the computation of $\mathbf{r}^{HR}$ has a complexity proportional to N card$(\mathcal{F})$, where card$(\mathcal{F})$ is the number of elements of $\mathcal{F}$ whereas, for a given Jacobian matrix $\mathbf{K}$, that of $\mathbf{K}^{HR}$ is proportional to N^2card$(\mathcal{F})+N$card$(\mathcal{F})$ [card$(\mathcal{F})$ + card$(\mathcal{I})$]. Eventually, the residual $\mathbf{r}[\mathcal{F}]$ and the Jacobian matrix $\mathbf{K}[\mathcal{F}, \mathcal{F} \cup \mathcal{I}]$ are computed over the RID. The lower the value of N and card$(\mathcal{F})$, the lower the computational complexity of the hyper-reduced arc-length equations.

Section 6 investigates the constructions of the reduced bases in the following cases:

- (i): Vector $\mathbf{Q}$ contains the simulation data related to $\mathbf{u}$ solely;
- (ii): in $\mathbf{V}$ two reduced bases, generated for $\mathbf{u}_t$ and $\mathbf{u}_b$ separately, are merged;
- (iii): in $\mathbf{Q}$ the simulation data related to $\mathbf{u}_t$ and $\mathbf{u}_b$ are merged, before computing $\mathbf{V}$.

6. Numerical results and discussion

6.1. Hyper-elastic buckling

In the sequel the finite element simulation of structures subjected to post-buckling is considered (see [38, 39] for details about post-buckling). This section demonstrates the robustness of the hyper-reduced arc-length method through a simple example in the framework of finite elastic strains. Focus is made on reduced-matrices $\mathbf{K}^{HR}$ when it is ill-conditioned.

Let us consider the highly-nonlinear buckling beam problem subjected to plain strain loading. The beam is parameterized by its slenderness, i.e. the ratio of length over height. The length is kept constant ($L = 200$ mm) and the slenderness is monitored by the height $\mu \in [8, 14]$. A morphing is applied to a reference mesh so as to generate a geometry corresponding to a given slenderness. The position vector $\mathbf{x}$ reads, accordingly:

$$\mathbf{x} = \left\{ \begin{array}{c} x_1 \\ \mu x_2 \end{array} \right\}, \tag{27}$$

where $x_1 \in [0, L]$(mm) and $x_2 \in [0, 1]$(mm) are coordinates in the reference mesh. The mesh is made of 295 linear elements (720 DOFs). The beam is fully clamped on one of its extremity while a pressure is applied on the opposite side, as shown in Figure 2.

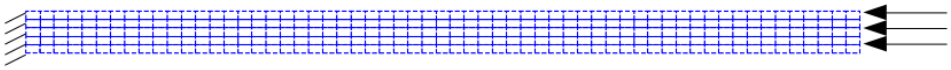

Figure 2: Meshed beam and boundary conditions.

The Young modulus for this simulation is $E = 210000$ MPa and the Poisson coefficient $\nu = 0.3$. The material follows the hyper-elastic Saint-Venant-Kirchhoff model:

$$\left\{\begin{array}{rl} \text{Deformation gradient tensor:} & \underset{\sim}{F} = \underset{\sim}{I} + \underset{\sim}{\nabla}\boldsymbol{v} \\ \text{Green-Lagrange strain tensor:} & \underset{\sim}{E} = \frac{1}{2}(\underset{\sim}{F}^T \cdot \underset{\sim}{F} - \underset{\sim}{I}) \\ \text{Constitutive law:} & \underset{\sim}{S} = \underset{\sim\sim}{\mathbb{C}} : \underset{\sim}{E} \\ \text{Cauchy stress:} & \underset{\sim}{\sigma} = \det^{-1}(\underset{\sim}{F})\ \underset{\sim}{F} \cdot \underset{\sim}{S} \cdot \underset{\sim}{F}^T \\ \text{Internal forces:} & f_i^{int} = \int_\Omega \frac{1}{2}(\underset{\sim}{\nabla}\boldsymbol{\phi}_i + \underset{\sim}{\nabla}^T\boldsymbol{\phi}_i) : \underset{\sim}{\sigma}\, d\Omega, \qquad i = 1, \dots \mathcal{N}, \end{array}\right. \tag{28}$$

where Ω denotes the current configuration. Simulation data for the training phase are generated for four sampling points in the parameter space: $\mu = 8$, 9, 10, 11. In the HR method it is common to make one single SVD on one global snapshot matrix that contains all the simulation results. Use is made of four simulations to apply separately a singular value decomposition on each of them hence four reduced bases are created. The resulting bases are then concatenated with each other without orthogonalization to create the reduced base:

$$\mathbf{V} = [\mathbf{V}^{(1)}, \mathbf{V}^{(2)}, \mathbf{V}^{(3)}, \mathbf{V}^{(4)}]. \tag{29}$$

Since the bases $\mathbf{V}^{(i)}$ are not orthogonal to each other, $\mathbf{V}$ is not orthogonal. Moreover $\mathbf{V}$ contains modes that are very similar to each other since the geometrical parameters are not too far from each others, and therefore the hyper-reduced tangent matrix $\mathbf{K}^{HR}$ is nearly singular. Nevertheless, the ill-conditioned system is kept as it is, to underline the robustness of the approach. If a linear system is ill-conditioned its response will vary a lot with respect to a small perturbation in the data. Let us consider a linear system with a positive-definite square matrix $\mathbf{A}$, a vector $\mathbf{b}$ and the unknown vector $\mathbf{u}$. If $\mathbf{A} \cdot \mathbf{u} = \mathbf{b}$ and $\mathbf{A} \cdot \mathbf{u}' = \mathbf{b}'$ one obtains, with $\Delta\mathbf{u} = \mathbf{u}' - \mathbf{u}$ and $\Delta\mathbf{b} = \mathbf{b}' - \mathbf{b}$:

$$\frac{||\Delta\mathbf{u}||_2}{||\mathbf{u}||_2} \leq \kappa(\mathbf{A}) \frac{||\Delta\mathbf{b}||_2}{||\mathbf{b}||_2}, \tag{30}$$

where the condition number $\kappa(\mathbf{A})$ is defined by:

$$\kappa(\mathbf{A}) = ||\mathbf{A}||_2 \times ||\mathbf{A}^{-1}||_2 = \frac{\sigma^A_{max}}{\sigma^A_{min}}, \tag{31}$$

and σ^A_{max}, σ^A_{min} are the highest (respectively, the lowest) eigenvalue of $\mathbf{A}$. The bigger the condition number, the less precise the solution ($\mathbf{u}$ in this case) will be.

Herefater, the DEIM is applied on the global reduced base $\mathbf{V}$ in order to select the nodes of the RID, enforcing $\mathcal{F} = \mathcal{P}$. In the following example no stress base was created. In the online test, the height takes on the value $\mu = 13.2$ mm. The reduced buckling beam at the end (red) and in initial position (blue) are shown in Figure (3).

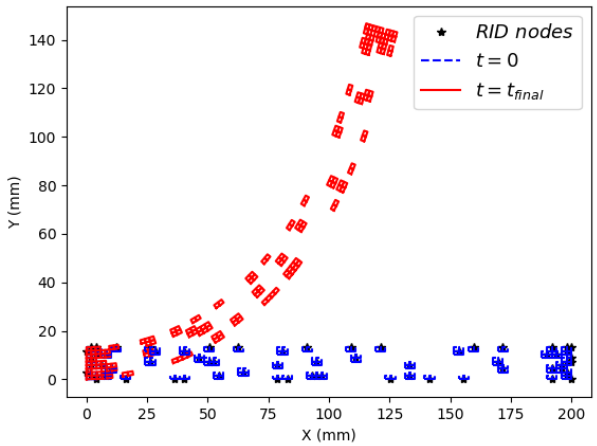

Figure 3: Hyper-reduced model at $t = 0$ (blue) and at t=t_{final} in red, for height $\mu = 13.2$ mm.

Here, the RID corresponds exactly to the elements attached to the selected node by the DEIM ($\mathcal{F} = \mathcal{P}$). The vertical displacement of the node at the bottom right, denoted M is plotted in Figure 4 as a function of the applied load. The nonlinear response due to buckling appears for a limit load equal to 1250 N and 1200 N when the FOM and the HROM are used, respectively. To check the accuracy of the proposed hyper-reduced arc-length algorithm, a FOM is run with the same parameter. The FOM and HROM responses are shown in Figure (4a). The exact error on the total displacement field is calculated by the quantity :

$$\eta = \frac{||\mathbf{u}_{HROM} - \mathbf{u}_{FOM}||_2}{||\mathbf{u}_{FOM}||_2}. \tag{32}$$

The later is represented in Fig. (4b).

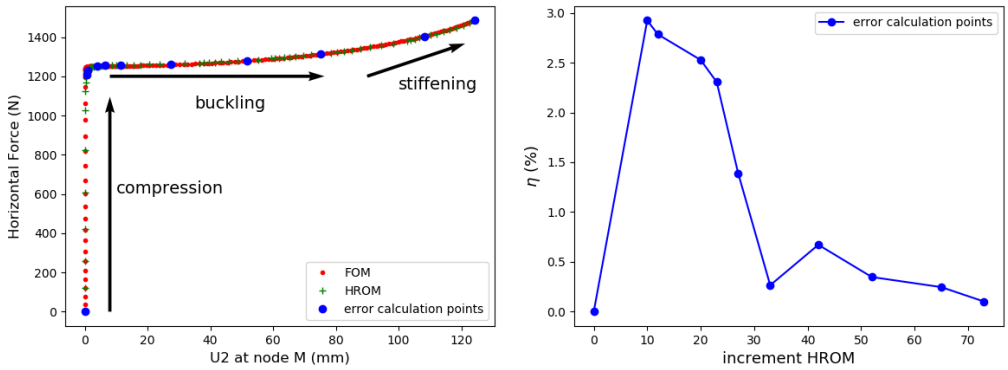

(a) (b)

Figure 4: (a) Load [N], as a function of the vertical displacement [mm] at point M, with $\mu = 13.2$. (b) Error estimate (%) as a function of the increments of the HROM simulation.

It has been observed that the condition number of $\mathbf{K}^{HR}$ evolves during the simulation, but remains very large (around 10^{16}), and, accordingly, $\mathbf{K}^{HR}$ is nearly singular. The robustness of the algorithm is warranted by the additional ellipse equation (25d) which prevents the divergence of the response since the latter must be contained within in the circle. Furthermore, for every loading increment the error stays between 0.1% and 2.9%. The largest error is observed when buckling occurs. Even in such strongly-nonlinear problem with ill-conditioned tangent matrix, convergence is obtained after a few iterations at each loading increment. These numerical results emphasize the robustness of the proposed hyper-reduced arc-length algorithm.

6.2. Limit load prediction for a simple elasto-plastic problem

To illustrate the assets of hyper-reduced arc-length algorithm one proposes a nonlinear problem that involves finite strains and plasticity. Let's consider a 3D thick wall pipe under internal pressure with a pure plastic behaviour. The material constitutive equations are

given below:

$$\left\{\begin{array}{rl}
\text{Strain gradient decomposition:} & \underset{\sim}{F} = \underset{\sim}{R}.\underset{\sim}{U} \\
\text{Deformation rate:} & \underset{\sim}{L} = \dot{\underset{\sim}{F}}.\underset{\sim}{F}^{-1} \\
\text{Stretch rate:} & \underset{\sim}{D} = \frac{1}{2}(\underset{\sim}{L} + \underset{\sim}{L}^{-T}) \\
\text{Local strain rate:} & \dot{\underset{\sim}{e}} = \underset{\sim}{R}^{T}.\underset{\sim}{D}.\underset{\sim}{R} \\
\text{Elastic/plastic partition:} & \underset{\sim}{e} = \underset{\sim}{e}^{e} + \underset{\sim}{e}^{p} \\
\text{Constitutive law:} & \underset{\sim}{S} = \underset{\approx}{\mathbb{C}} : \underset{\sim}{e}^{e} \\
\text{Relation with global Cauchy stress:} & \underset{\sim}{\sigma} = \det{}^{-1}(\underset{\sim}{F})\ \underset{\sim}{R}.\underset{\sim}{S}.\underset{\sim}{R}^{T} \\
\text{Second invariant of the stress tensor :} & J_2(\underset{\sim}{\sigma}) = \sqrt{\frac{3}{2}\ dev(\underset{\sim}{\sigma}) : dev(\underset{\sim}{\sigma})} \\
\text{Yield stress:} & R_0 \\
\text{Yield function:} & f(\underset{\sim}{\sigma}, R) = J_2(\underset{\sim}{\sigma}) - R_0 \\
\text{Internal forces:} & f_{int\,i} = \int_\Omega \frac{1}{2}(\underset{\sim}{\nabla}\boldsymbol{\phi}_i + \underset{\sim}{\nabla}^{T}\boldsymbol{\phi}_i) : \underset{\sim}{\sigma}\, d\Omega,\ i = 1, \dots\ \mathcal{N}
\end{array}\right. \tag{33}$$

The Young modulus used for this simulation is $E = 200000$ MPa, the Poisson coefficient is $\nu = 0.3$ and the elasticity limit is $R_0 = 400$ MPa. As it can be seen in the material constitutive equations give before there is no hardening in this example. The considered pipe is fully clamped on each side and undergo internal pressure.

In the present work, a parametric study is conducted by varying the geometric parameters and determining the pipe's critical pressure. The pipe length is fixed hereafter to $L = 300$mm whereas the thickness and external radius vary. The full-order model is made up of $9,180$ linear hexahedra ($\mathcal{N} = 37,536$ DOF, see Fig. 5) and an updated Lagrangian formulation is used.

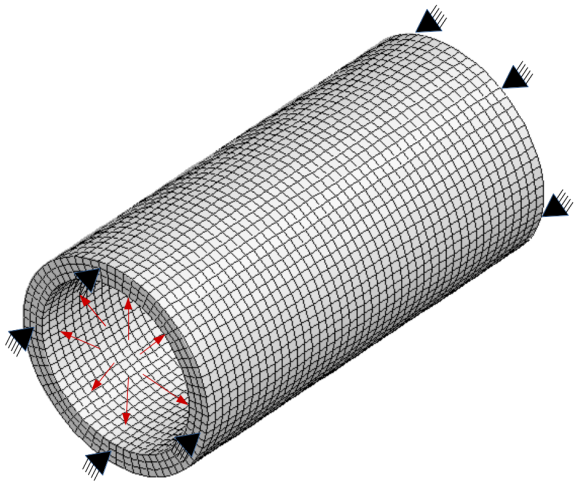

Figure 5: Meshed pipe with boundary conditions.

As announced in section (5), two linear systems are solved for a given linearized residual. Many choices for the reduced base are possible. The snapshot matrices $\mathbf{Q}$, $\mathbf{Q}_t$ and $\mathbf{Q}_b$ contain, respectively, the solution $\mathbf{u}$, $\mathbf{u}_t$ and $\mathbf{u}_b$ for each point in $\mathcal{D}_{train}$, and at any time the equilibrium path is reached. Hereafter, results obtained for three different reduced bases $\mathbf{V}_A$, $\mathbf{V}_B$ and $\mathbf{V}_C$ are compared. The later are constructed as follow:

$$\text{reduced base } \mathbf{V}_A: \quad \left\{ \mathbf{Q} = \mathbf{V}_A.\mathbf{\Sigma}_A.\mathbf{W}_A^T + \mathbf{R}_A, \quad \|\mathbf{R}_A\|_2^2/\|\mathbf{Q}\|_2^2 < \epsilon_{tol}, \right. \tag{34a}$$

$$\text{reduced base } \mathbf{V}_B: \quad \left\{ \begin{array}{rcll} \mathbf{Q}_t & = & \mathbf{V}_t.\mathbf{\Sigma}_t.\mathbf{W}_t^T + \mathbf{R}_t, & \|\mathbf{R}_t\|_2^2/\|\mathbf{Q}_t\|_2^2 < \epsilon_{tol}, \\ \mathbf{Q}_b & = & \mathbf{V}_b.\mathbf{\Sigma}_b.\mathbf{W}_b^T + \mathbf{R}_b, & \|\mathbf{R}_b\|_2^2/\|\mathbf{Q}_b\|_2^2 < \epsilon_{tol}, \\ \mathbf{V}_B & = & [\mathbf{V}_t,\ \mathbf{V}_b], & \end{array} \right. \tag{34b}$$

$$\text{reduced base } \mathbf{V}_C: \quad \left\{ \begin{array}{rcll} \mathbf{Q}_{tb} & = & [\mathbf{Q}_t,\ \mathbf{Q}_b], & \\ \mathbf{Q}_{tb} & = & \mathbf{V}_C.\mathbf{\Sigma}_C.\mathbf{W}_C^T + \mathbf{R}_C, & \|\mathbf{R}_C\|_2^2/\|\mathbf{Q}_{tb}\|_2^2 < \epsilon_{tol}. \end{array} \right. \tag{34c}$$

Four offline classical finite element simulations are carried out with different values of thickness and external radius. An online target simulation is defined with another couple (thickness, external radius). This online simulation is performed three times with the three different reduced bases $\mathbf{V}_A$, $\mathbf{V}_B$ and $\mathbf{V}_C$. Table (1) gives the parameter values used in the simulations. The later follow the thickest pipes for deep offshore. It is emphasized that the online simulation lies beyond the parametric-training region.

A criterion is now introduced in order to stop the numerical simulations and to estimate the critical pressure. As a rule, the computation of the equilibrium path is stopped whenever the pressure has decreased by more than 4% from its maximum value. Figure (6)

	External radius (mm)	Thickness(mm)
Offline	75	15
Offline	80	20
Offline	80	15
Offline	75	20
Online	*70*	*10*

Table 1: Parameters for offline ($\mathcal{D}_{train}$) and online simulations

shows the local pressure as a function of the norm of the displacement along an arbitrary node in the middle of the plane.

The red and blue arrows spot the values of the critical pressure and the corresponding displacement for a point on the external skin of the pipe in the mid-plane. The values are respectively for the FOM simulation : (0.9 mm ; 115,4 MPa) and HROM simulation : (1,3 mm ; 114,94 MPa). The error is estimated after the simulation has been completed. In order to have the exact error, a FOM simulation with the same parameters as used in the HROM simulation is carried out. Maps of the displacement component U_1 is shown in Figure 7 as computed in the RID and along the full mesh. The small part of the reduced mesh on the left of the image contains the point used to plot the loading curve in Figure 6. Details about the construction of the RID are given in appendix 9. It is emphasized that the construction of the RID is empirical and depends on the considered problem.

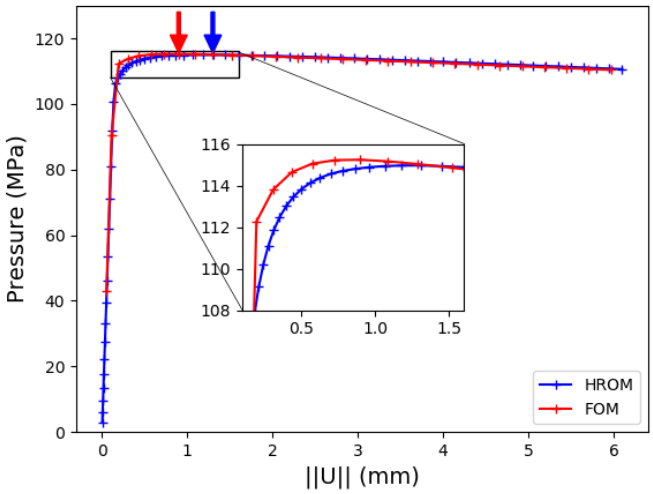

Figure 6: Internal pressure (MPa) as a function of the norm of the displacement (mm) of a node in the middle plane (offline in blue and online in red). Computation carried out using the reduced base matrix $\mathbf{V}_B$. The limit load is indicated by the arrow.

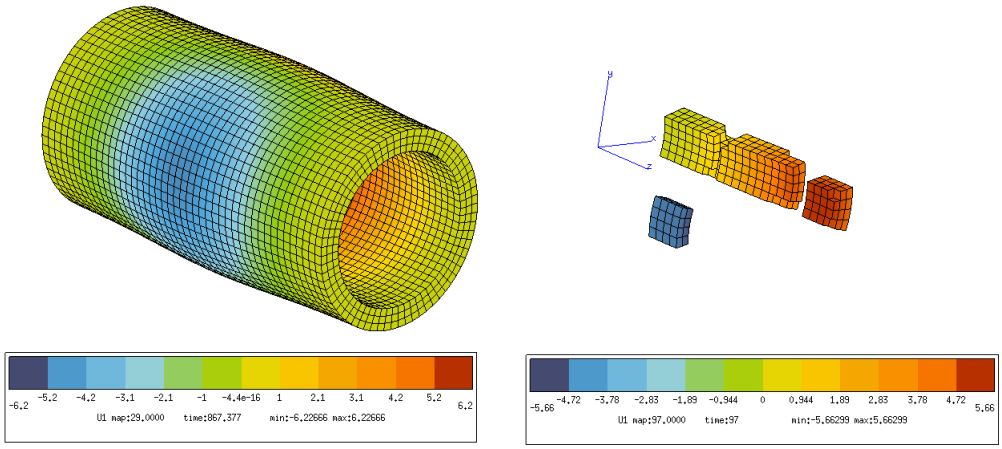

(a) (b)

Figure 7: Displacement component U_1 (mm) computed on the full mesh (a) and on the RID (b) using the reduced base matrix $\mathbf{V}_B$.

In the following, the absolute error relative to the displacement U_1 is defined by:

$$\varepsilon^{U_1} = \max\left\{\frac{|\mathbf{U_1}^{HROM} - \mathbf{U_1}^{FOM}|}{\max|\mathbf{U_1}^{FOM}|}\right\}, \tag{35}$$

where the max operator in the denominator has been introduced to take into account the fact that U_1 might be zero. Similar error criteria are considered for the other displacement and stress components. Table 2 reports the errors for the 3 displacement components and the six stress components, for each of the three reduced bases, i.e. $\mathbf{V}_A$, $\mathbf{V}_B$ and $\mathbf{V}_C$. The values in bold, corresponding to the most accurate computations, indicate that base $\mathbf{V}_A$ gives the best results as compared to the two other bases, while also using standard simulation outputs. Therefore, the construction method for this base is used in the rest of this work.

	$\mathbf{V}_A$	$\mathbf{V}_B$	$\mathbf{V}_C$
N	**8**	11	9
$\text{card}(\mathcal{F})$	**1 830**	2 985	3 009
$\varepsilon^{U1} = \varepsilon^{U2}$	3.80%	1.91%	**0.45**%
ε^{U3}	**3.84**%	4.17%	4.81%
$\varepsilon^{\sigma^{11}} = \varepsilon^{\sigma^{22}}$	**3.46**%	7.63%	10.64%
$\varepsilon^{\sigma^{33}}$	**2.75**%	6.61%	6.69%
$\varepsilon^{\sigma^{31}} = \varepsilon^{\sigma^{32}}$	**5.63**%	9.94%	9.97%
$\varepsilon^{\sigma^{12}}$	**5.63**%	16.44%	19.05%

Table 2: Error relative to the displacement and stress components, for different constructions of the reduced base.

6.3. Greedy sampling and validity domain for a realistic problem

In this subsection, a parametric study is carried out on an elbowed pipe. Many studies have been carried out on elbow pipes [22, 23, 40]. The geometric parameters are chosen according to the work of [22]. This study focuses on determining the critical internal pressure this structure can sustain. Compare to the previous problem, the geometry as well as the mesh and boundary conditions are modified. Four geometric parameters are considered: the thickness e, the external radius R_{ext}, the curvature radius r_{curv} and the angle of elbow α. As in the previous section a morphing method is used to modify the mesh. A sensitivity-analysis of each parameter is carried out by varying each value of $\pm 5\%$ (see Table 3). The mesh used in this study has $16,000$ linear 8-nodes elements resulting in $24,633$ nodes and $\mathcal{N} = 73,899$ DOFs. Both symmetries of the problem have been taken

into account hence only one quarter of the pipe is considered. The mesh is represented in Figure 8. Additionally, an error indicator developped in the context of small strain [41] is coupled with a greedy algorithm in order to reduce the amount of training data. In small strain setting, the equilibrium equation is a linear equation and is fulfilled, in its weak form, by the stress computed during the offline phase. It turns out that the related reduced bases $\mathbf{V}^\sigma$ is a convenient subspace for stresses. For problems in the more general context of finite strain, the equilibrium equation strongly depends on the displacement in the domain Ω and is a nonlinear equation. Nevertheless, it is assumed in the following that the training set $\mathcal{D}_{train}$ is large enough, and is able to represent accurately both the displacement fields and the stress field via their respective reduced bases $\mathbf{V}$ and $\mathbf{V}^\sigma$.

R_{ext} (mm)	r_{curv} (mm)	e (mm)	α (°)
39.9	114	4.75	42.75
44.1	126	5.25	47.25

Table 3: Range of geometrical parameters, for the training set of simulation data.

In the following, consistency criteria are introduced and used as error indicator for the sampling of the parameter space by a greedy algorithm. Each time a hyper-reduced arc length simulation predicts a displacement by using $\mathbf{V}$, the projection on $\mathbf{V}^\sigma$ of the related stresses is expected to yield an accurate solution. The error indicator is accordingly defined by:

$$\varepsilon^* = \min_{\boldsymbol{\gamma}^*} \frac{||\sigma^{HR} - \mathbf{V}^\sigma[\mathcal{F},:] \cdot \boldsymbol{\gamma}^*||_2}{||\sigma^{HR}||_2}, \tag{36}$$

$$\text{achieved with:} \quad \boldsymbol{\gamma}^* = \left(\mathbf{V}^\sigma[\mathcal{F},:]^T \cdot \mathbf{V}^\sigma[\mathcal{F},:]\right)^{-1} \cdot \mathbf{V}^\sigma[\mathcal{F},:]^T \cdot \sigma^{HR}, \tag{37}$$

where $\boldsymbol{\gamma}^*$ is the reduced coordinate vector related to the Gappy POD applied to the stress. This vector minimizes the gap between the stress field obtained with the hyper-reduced arc length simulation, σ^{HR}, and the its projection on $\mathbf{V}^\sigma$ over the RID. The product $\mathbf{V}^\sigma \cdot \boldsymbol{\gamma}^*$ is the recovered stress over Ω related to the Gappy POD. Because of the finite strains involved in the equilibrium path, we have not established a formal relationship between the error indicator and the true error on the displacements. But this relationship exists for standard materials undergoing small deformations [41]. A greedy algorithm is accordingly applied to construct the global reduced base (see [11]):

(i) the sampling point in the parameter space for which the error is maximal is first obtained, according to the error estimator based on the HR simulation;

(ii) second, the FOM simulation data relative to this point is included in the training set for the global reduced base, and the reduced base is computed again;

(iii) hyper-reduced predictions and error predictions are then performed for all sampling points.

Note that the first sampling point in the parameter space is the center of the hyper-cube.

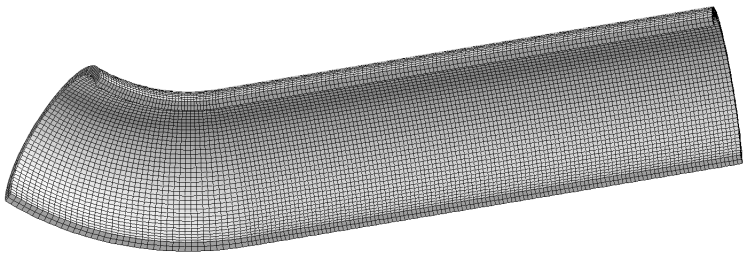

Figure 8: Elbowed pipes meshed.

The parametric space is regularly sampled on a $m \times m \times m \times m$ grid where m is the number of values each parameter can take. In the present case, $m = 2$ generating 16 simulations to which is added the first sampling point at the center of the hyper-cube resulting in 17 simulations. After applying five times the greedy algorithm, five FOM simulations are added to the training set. The 12 other hyper-reduced simulations where thus required to certify the model. The 12 related simulation data are denoted validation data in the following. Figure (9) shows the evolution of the error indicator during the iterations of the greedy algorithm. The training set that is selected with this method is indicated by the black numbers.

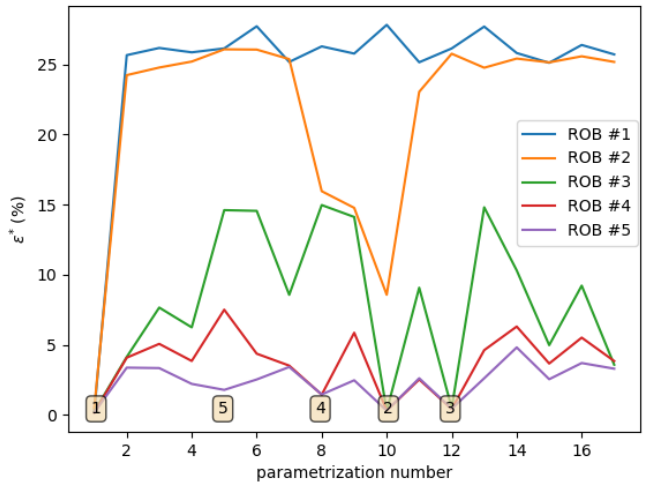

Figure 9: Error indicator for the different hyper-reduced arc length simulations over the sampling point of the parameter space, where the ROB number $i+1$ is obtained after the i^{th} iteration of the greedy algorithm. The brown squares with numbers inside indicate the sampling point inserted in the training set $\mathcal{D}_{train}$ and their iteration index.

.

The greedy algorithm is found to be very efficient. No more than five iterations of the algorithm are needed in the present study, resulting in a global error of less than 5%. The resulting RID is composed of $8,511$ nodes. The last reduced base $\mathbf{V}$ contains $N = 27$ empirical modes, with $\epsilon_{tol} = 1e^{-8}$ and $N^3 < \mathcal{N}$. The reduced base $\mathbf{V}^\sigma$ contains 50 empirical modes. The RID construction, shown in Figure 10, follows the procedure in Appendix 9. The resulting HROM is denoted HROM5-27-50 in the the following. As expected, plasticity localizes at the curvature where stress concentration occurs. Note that the obtained RID is rather large compared to the one that is usually seen with standard hyper-reduction methods. This should be explained by the loss of ellipticity in the equations, encountered in limit load problems.

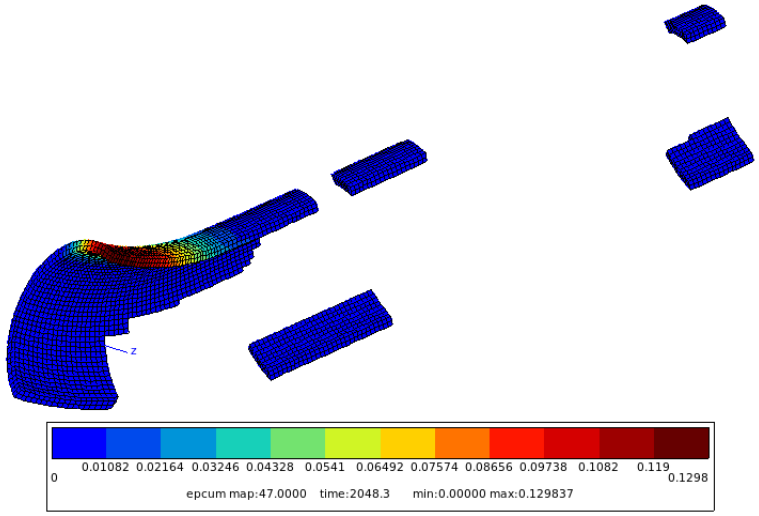

Figure 10: Cumulated plasticity on the RID of the elbowed pipe.

The error indicator is now compared with one based on the full-order model prediction, in order to investigate its reliability. This time, the simulation of the loading path stops when a decrease of 1% of the pressure is observed, compared its maximal value. Note however that a small error on the limit load estimate may induce a much larger error on the displacement. Therefore, displacement fields are compared according to their angle with the solution obtained with the FOM. The later reads:

$$\Theta = \cos^{-1}\left\{\frac{\left(\mathbf{u}^{HR}[\mathcal{F}]\right)^T \cdot \mathbf{u}^{FOM}[\mathcal{F}]}{||\mathbf{u}^{HR}[\mathcal{F}]||_2||\mathbf{u}^{FOM}[\mathcal{F}]||_2}\right\} \in [0, \frac{\Pi}{2}]. \tag{38}$$

The angle Θ is computed for each of the 17 simulations as it is necessary to evaluate the error estimator. The correlation between Θ and ε^*, show a linear relation between Θ and ε^*, except for two points are far from the zone of interest delimited by an error of 25% (see Figure 11). The computation of the error angle Θ requires all FOM simulations, contrary to the error estimator ε^*. For the later, a reduced base on the stress field is sufficient. Therefore, this error estimator will be used in the rest of this work. Using HROM5-27-50, one may now carry out HROM calculations on a finer grid of the parameter space. The parametric space is re-sampled along a $3\times3\times3\times3$ grid, resulting in 81 HROM simulations and to the error map represented in Figure (12).

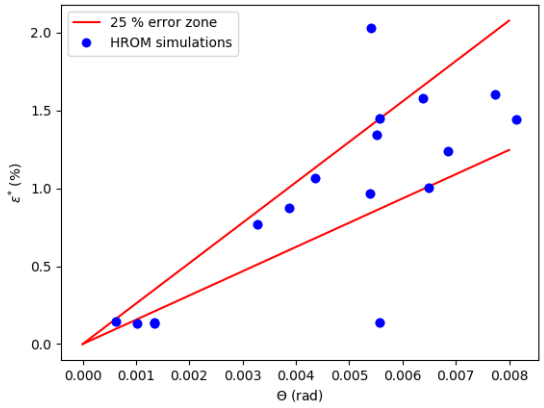

Figure 11: Error indicator Θ (rad) versus error estimator $\varepsilon^*(\%)$ on the 17 HROM simulations.

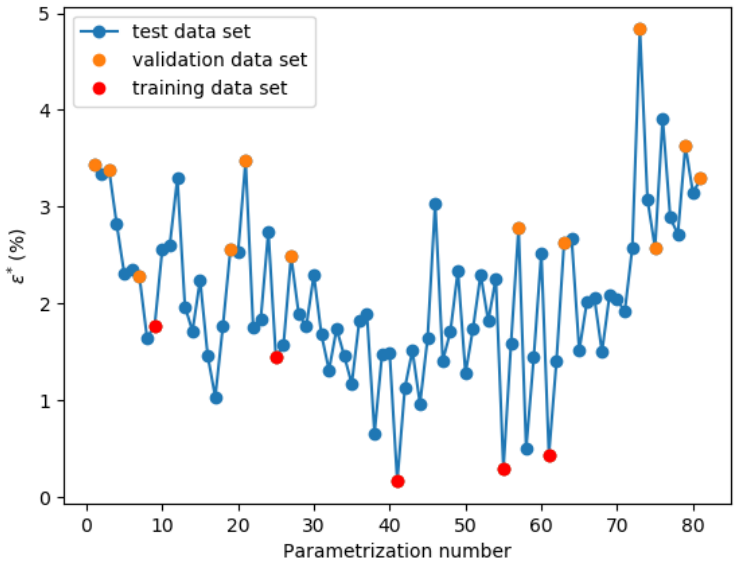

Figure 12: Error estimate ε^* for the 81 HROM simulations. The red dots represent the training data set used to created the reduced base, the orange dots are the validation data set used to certify our model and the blue dots are the test data set.

The global minimum of the error estimate is a simulation from the training set and

the global maximum is a simulation from the validation data set. The values of the parameters for the test data set lie between the minimum and maximum values of the parameters in the validation data set. The error indicator is inferior to 5%, highlighting how accurate is the hyper-reduced model for the interpolation. Then one can continue the stability analysis with the so developped hyper reduced model (HROM5-27-50). The most sensitive parameter is determined using the parallel coordinate plot method [42]. A parallel coordinate plot is introduced (Figure 13). The four first coordinates are relative to the parameters (thickness, external radius etc.) whereas the last one is the simulation output of interest (i.e. the critical pressure). The red lines in Figure (13a) are related to sampling points in the parameter space which lead to a high critical pressure, in the present case P_c^{max} $+0\%$ -2.5%. If all red lines intersect at the same parameter value, for a specific set of parameters, that parameter is strongly sensitive with respect to the simulation output. According to graph (13a), the external radius as well as the thickness are the parameters most sensitive to the highest critical pressure. Obviously, a small external radius and a big thickness. results in a high critical pressure, as shown by the red lines in Fig. (13a)). To estimate how robust the proposed model is, a coordinate plot is represented, again, in Fig. (13b) to determine which parameter influence the error indicator the most. The map is defined by relative variations of $+0\% - 25\%$ on the outputs. The external radius, the thickness and the radius of curvature influence most the error indicator. The external radius and the radius of curvature are not independent in the chosen parametrization. Indeed the curvature radius is defined according to the middle line of the pipe. Therefore the larger the external radius, the smaller the radius of curvature of the upper skin of the pipe.

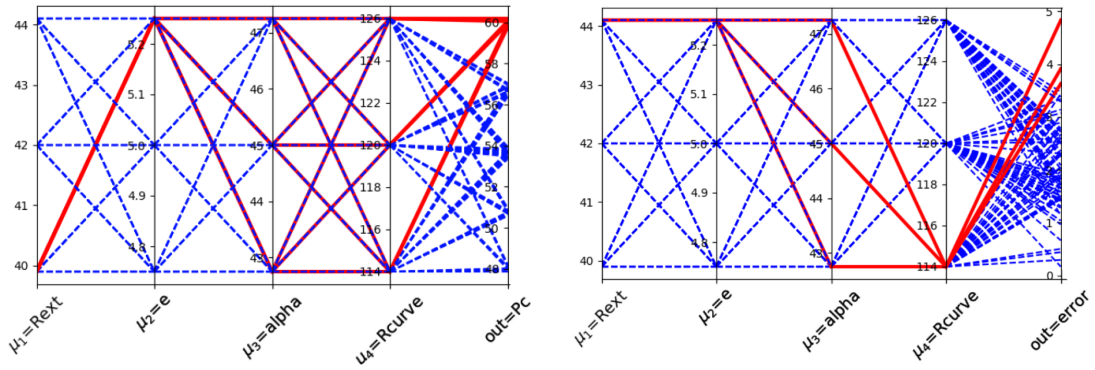

(a) (b)

Figure 13: Parallel coordinates plots. Each axis represents a parameter except for the output, indicated last one on the right along the x-axis. (a) Critical pressure. (b) Error estimate.

The training set is made of five FOM simulations. Denoting $CPU_{FOM} = 5672$s the computational time of the FOM simulations, and $CPU_{HR} = 1035$s that of the HROM simulations, the speed-up, defined by:

$$\text{speed-up} = \frac{CPU_{FOM} \times 81}{CPU_{HR} \times 81 + CPU_{FOM} \times 5}, \tag{39}$$

is about 4.1, slightly lower than the direct speed up : $CPU_{FOM}/CPU_{HROM} = 5.48$.

By varying the thickness and the radius of curvature and fixing the others parameters to $Rext = 42mm$ and $\alpha = 45$ °, a domain of validity is defined, where the error indicator is inferior to 10%. In that case, the hyper-reduced model HROM5-27-50 does not only interpolate but also extrapolate training data. A variation of ±25% of the thickness and of the curvature radius is applied and the parametric space is divided in a grid of 10×10 points, resulting in 100 HROM simulations. Figure (14) shows that the HROM model has a quite a large validity domain in spite of its construction, which uses only 5 high fidelity simulations.

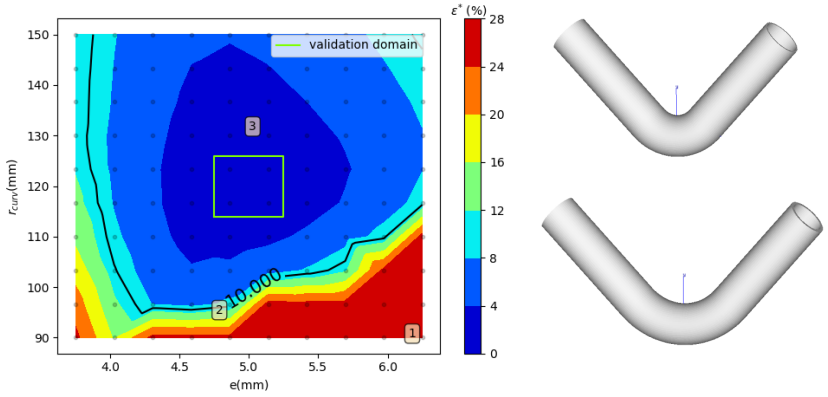

(a) (b)

Figure 14: Map of the error estimate for the hyper-reduced model with isocontour equal to 10%, for varying curvature radius and thickness. Each black point in the background represents a HROM simulation and the green square represents the domain of the validation dataset (on the left). Representation of the pipe with minimum and maximum values of both parameters simultaneously (on the right).

The parameters for three test points in the parameter space, indicated on Figure 14.a, are given in table 4. The error on the von Mises stress corresponding to the three test points indicated by the black numbers in Figure 14.a may be calculated on each Gauss point of the RID and of the full mesh, once the gappy POD has been applied to stresses. A

Number	r_{curv} (mm)	e mm)
1	90	6.25
2	96.66	4.86
3	130	5.13

Table 4: Set of parameters of the three simulations indicated in Figure 14

reference computation has been carried out with the FOM for these three configurations. The correlation curves for stress predictions are shown in Figure (15).

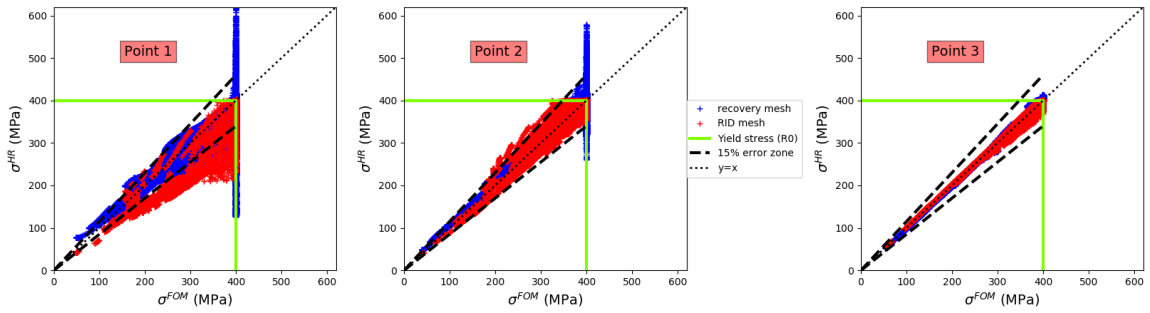

Figure 15: Error for the von Mises stress, for test points 1, 2, 3 in the parameter space (table 4). Each marker represents a gauss point, the x-axis is the reference value and the y-axis the value computed with the hyper-reduced method. Red points are related to the prediction in the RID. Blue points are related to the gappy POD for the stress recovery over Ω.

As shown in Figure (15), the prediction of the equivalent stress on the RID is more accurate than on the full mesh. Outside the RID, the gappy POD gives stresses that violate the limit R_0 enforced by perfect plasticity. In the RID, the stresses are obtained by integrating the constitutive relations. Therefore they are plastically admissible. These results confirm that the proposed error indicator is relevant in this example. In order to show the robustness of the HROM5-27-50 model, variations of the two other parameters (external radius and angle) have also been considered. Constant values have been given to the curvature radius (120mm) and the thickness (5mm). As previsously, the parameters vary within $\pm 25\%$ and the parametric space is divided in a grid of 10×10 points. The assumed validity domain given by an error indicator less than 10% is once again quite large, which shows the robustness of the hyper-reduced arc length method (Fig. 16).

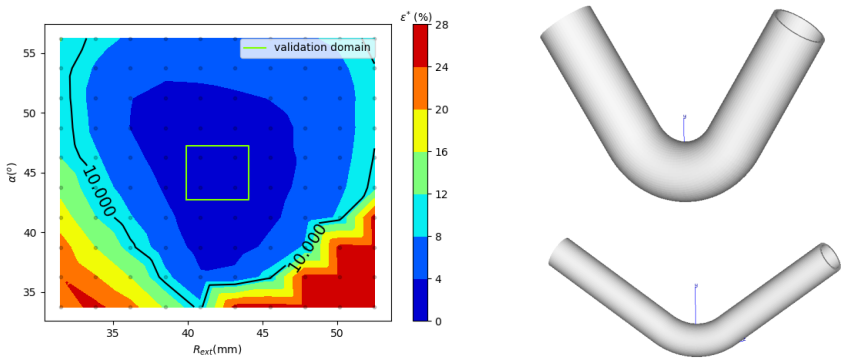

(a) (b)

Figure 16: Map of the error estimate for the hyper-reduced model with isocontour equal to 10% for varying external radii and angles (a). Each black point in the background represents a HROM simulation and the green square represents the domain of the validation dataset. (b) Representation of the pipe with minimum and maximum values of both parameters simultaneously.

7. Speed-up

The previous simulations have been carried out on 24 processors. In the HR simulations, most of the CPU time is spent for the integration of the material constitutive law and the computation of the internal reactions. The later represents 77% of the computational time while the construction of the hyper-reduced matrix represents 2% and the solving time of the linear system represents 3%. The rest of the time is used for other tasks. Accordingly, the size of the RID plays an important role on the speed-up. This shows the robustness of the method despite the moderate speed-up, equal to 5.5. In order to increase the speed-up less modes in the HR model have been used, as well as less RID elements. In the present section, a hyper-reduced model, denoted HROM5-9-73 created with the 5 FOM simulations and made of 9 displacement modes, 73 stress modes modes and a RID of 8,694 DOFs is considered. This model is used to simulate the problem represented by point 2 in Figure (14). Figure (17) shows the RID now used, to be compared with that of HROM5-27-50 (Figure 10). The much-reduced RID contains $2,898$ nodes instead of $8,511$ nodes as in HROM5-27-50. Numerical investigations show that the speed-up now equals 14.5. Enhancing the speed-up, however, leads to a larger error. With model HROM5-9-73 is around 30% instead 15% for model HROM5-27-50. Although the error of the stress field is twice larger, the error on the estimate for the limit load (about 47.1MPa with the FOM model) is less than 1%.

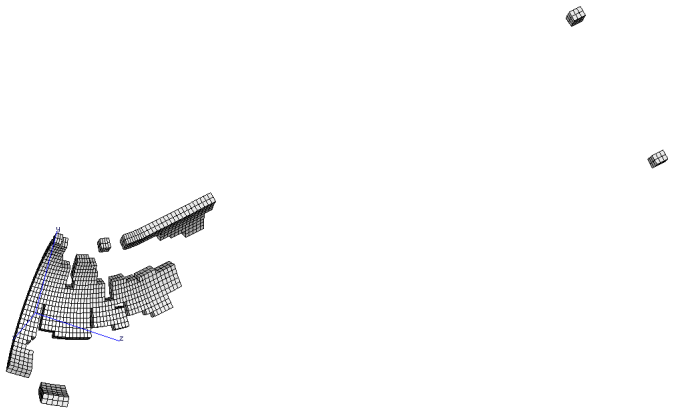

Figure 17: RID of HROM5-9-73.

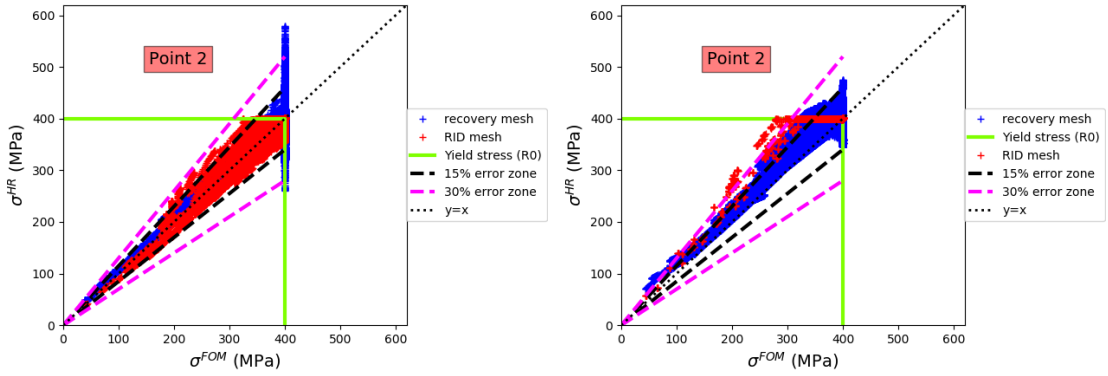

Figure 18: Error on the von Mises stress, for test points 2 in the parameter space. Each marker of the following graph represents a gauss point, the x-axis represents the reference value and the y-axis the value computed with the proposed method. Red point are related to the prediction in the RID. Blue points are related to the gappy POD for the stress recovery over Ω. (a) HROM5-27-50. (b) HROM5-9-73.

8. Conclusion

An extension to the hyper-reduced method based on a reduced integration domain has been introduced. It should be emphasized that "snap-back" phenomena [34], which go beyond the scope of this paper, are not addressed in the present work. It accurately predicts

buckling and yields accurate limit-loads, in the context of finite strain and elastoplastic behaviour. The method has been tested on an academic problem, that of a 2D hyper elastic buckling beam. In spite of a ill-conditioned tangent matrix, the algorithm shows good convergence properties, making use of the hyper reduced arc-length algorithm. Various constructions of the reduced base have been considered through the example of a straight pipe under internal pressure. The different contributions of each linear system to be solved have been taken into account to determined the best construction method of the reduced base. It has been found that the best ones uses standard simulation outputs to train reduced bases. Moreover, an error indicator based on the stress field has been proposed, and coupled with a greedy algorithm in order to choose snapshots that are simulated via finite element model. Using this estimator the domain of validity of the model has been determined for an elbowed pipe in a four dimensions-parametric space. The hyper-reduced model shows excellent results not only when interpolating data but also, for extrapolating (at least in a limited range beyond the training set). Our results show the efficiency and robusteness of the proposed strategy in terms of accuracy of the solution and of stability of the hyper-reduced algorithm. A promising result as well is the speed-up, between 4 and 14 in the examples studied.

9. Appendix: RID construction

To detail the construction of the RID, it is convenient to introduce two mathematical operators. The first one collects the degrees of freedom over a sub-domain Ω_α and is defined by:

$$\mathcal{C}(\Omega_\alpha) = \{i \in \{1, \ldots \mathcal{N}\}, \int_{\Omega_\alpha} \boldsymbol{\phi}_i^2 \, d\Omega > 0\}$$

The second one aggregates the support of the FE shape functions having their index in a set $\mathcal{L}$:

$$\mathcal{V}(\mathcal{L}) = \cup_{i \in \mathcal{L}} \text{supp}(\boldsymbol{\phi}_i), \quad \mathcal{V}(\mathcal{L}) \subset \Omega$$

The extension of this subdomain by adding n layers of connected elements reads:

$$(\mathcal{V} \circ \mathcal{C})^n \circ \mathcal{V}(\mathcal{L}).$$

The operator $\mathcal{V}$ is adapted to displacement fields, which are approximated by FE shape functions. A similar operator may be introduced for stresses. When collecting simulation data related to stresses, in the matrix $\mathbf{Q}^\sigma$, all stress components at all Gauss points are stored for all elements. Each row of $\mathbf{Q}^\sigma$ is related to one component of the stress tensor, at a Gauss point in an element. Then, the DEIM algorithm applied to $\mathbf{V}^\sigma$ gives a set of indices of components of the stress tensor, at some Gauss points, in some elements.

Denoted this set $\mathcal{P}^\sigma$ and denote $\mathcal{V}^\sigma(\mathcal{P}^\sigma)$ the support of the elements related to set $\mathcal{P}^\sigma$. Then, $\mathcal{V}^\sigma(\mathcal{P}^\sigma)$ is a subdomain of Ω.

In the second example, the RID construction is:

$$\Omega_A = (\mathcal{V} \circ \mathcal{C})^2 \circ (\mathcal{V}(\mathcal{P}) \cup \mathcal{V}^\sigma(\mathcal{P}^\sigma)) \cup \mathcal{V} \circ \mathcal{C} \circ \mathcal{V}(\{i_o\})$$

where i_o is the degree of freedom used to plot the load-displacement curve in Figure 7.

10. References

[1] S. Acharyya, s. Dhar, A complete gtn model for prediction of ductile failure of pipe, Journal of Materials Science 43 (2008) 1897–1909. doi:10.1007/s10853-007-2369-0.

[2] S. Volkwein, Proper orthogonal decomposition:theory and reduced-order modelling, Lecture notes, University of Konstanz, Department of Mathematics and Statistics.

[3] G. Kerschen, J.-C. Golinval, A. VAKAKIS, L. BERGMAN, The method of proper orthogonal decomposition for dynamical characterization and order reduction of mechanical systems: An overview, Nonlinear Dynamics 41 (2005) 147–169. doi:10.1007/s11071-005-2803-2.

[4] N. Aubry, P. Holmes, J. Lumley, E. Stone, The dynamics of coherent structures in the wall region of a turbulent boundary layer, Journal of Fluid Mechanics 192 (1988) 115 – 173. doi:10.1017/S0022112088001818.

[5] B. Almroth, F. Brogan, P. Stern, Automatic choice of global shape functions in structural analysis, AIAA Journal 16 (1978) 525–528. doi:10.2514/3.7539.

[6] M. Raissi, P. Perdikaris, G. Karniadakis, Physics-informed neural networks: A deep learning framework for solving forward and inverse problems involving nonlinear partial differential equations, Journal of Computational Physics 378. doi:10.1016/j.jcp.2018.10.045.

[7] F. Nguyen, S. Barhli, D. Muñoz, D. Ryckelynck, Computer vision with error estimation for reduced order modeling of macroscopic mechanical tests, Complexity 2018 (2018) 1–10. doi:10.1155/2018/3791543.

[8] T. Daniel, F. Casenave, N. Akkari, D. Ryckelynck, Model order reduction assisted by deep neural networks (rom-net), Advanced Modeling and Simulation in Engineering Sciences 7. doi:10.1186/s40323-020-00153-6.

[9] D. Ryckelynck, A priori hyperreduction method: An adaptive approach, Journal of Computational Physics 202 (2005) 346–366. doi:10.1016/j.jcp.2004.07.015.

[10] D. Ryckelynck, F. Vincent, S. Cantournet, Multidimensional a priori hyper-reduction of mechanical models involving internal variables, Multidimensional a priori hyper-reduction of mechanical models involving internal variables 225 (2012) 28–43. doi:10.1016/j.cma.2012.03.005.

[11] J. Fauque, I. Ramière, D. Ryckelynck, Hybrid hyper-reduced modeling for contact mechanics problems, International Journal for Numerical Methods in Engineering 115. doi:10.1002/nme.5798.

[12] G.-L. She, Y.-R. Ren, K.-M. Yan, On snap-buckling of porous fg curved nanobeams, Acta Astronautica 161 (2019) 475–484. doi:10.1016/j.actaastro.2019.04.010.

[13] A. Hamdaoui, B. Braikat, N. Tounsi, N. Damil, On the use of pade approximant in the asymptotic numerical method anm to compute the post-buckling of shells, Finite Elements in Analysis and Design 137 (2017) 1–10. doi:10.1016/j.finel.2017.08.004.

[14] C. Tsai, A. Palazotto, A modified riks approach to composite shell snapping using a high-order shear deformation theory, Computers and Structures 35 (1990) 221–226. doi:10.1016/0045-7949(90)90341-X.

[15] C. Tsai, A. Palazotto, Nonlinear and multiple snapping responses of cylindrical panels comparing displacement control and riks method, Computers and Structures - COMPUT STRUCT 41 (1991) 605–610. doi:10.1016/0045-7949(91)90172-I.

[16] W. Zhao, M. Chen, H. Chen, A novel trajectory interpolation algorithm for wedm - unit generalized arc length increment method, Procedia CIRP 6 (2013) 256–261. doi:10.1016/j.procir.2013.03.074.

[17] E. Riks, An incremental approach to the solution of snapping and buckling problems, Int. J. Solids Struct. 7 (1971) 1581–1599.

[18] M. Crisfield, A fast incremental/iterative solution procedure that handles "snap-through", Computers and Structures 13 (1981) 55–62. doi:10.1016/0045-7949(81)90108-5.

[19] E. de Souza Neto, Y. Feng, On the determination of the path direction for arc-length methods in the presence of bifurcations and 'snap-backs', Computer Methods in Applied Mechanics and Engineering - COMPUT METHOD APPL MECH ENG 179 (1999) 81–89. doi:10.1016/S0045-7825(99)00042-0.

[20] A. Akbari R., P. Kerfriden, S. Bordas, Scale selection in nonlinear fracture mechanics of heterogeneous materials, Philosophical Magazine 95 (2015) 3328–3347. doi:10.1080/14786435.2015.1061716.

[21] O. Allix, P. Kerfriden, P. Gosselet, On the control of the load increments for a proper description of multiple delamination in a domain decomposition framework, International Journal for Numerical Methods in Engineering 83 (2010) 1518 – 1540. doi:10.1002/nme.2884.

[22] Q. Wang, W. Zhou, Burst pressure models for thin-walled pipe elbows, International Journal of Mechanical Sciences 159. doi:10.1016/j.ijmecsci.2019.05.027.

[23] M. Khalaj Khalajestani, M. Bahaari, A. Salehi, S. Shahbazi, Predicting the limit pressure capacity of pipe elbows containing single defects, Applied Ocean Research 53 (2015) 15–22. doi:10.1016/j.apor.2015.07.002.

[24] U. Zerbst, Al, Chapter 5 - the model parameters.

[25] K. Carlberg, J. Cortial, D. Amsallem, M. Zahr, C. Farhat, The gnat nonlinear model reduction method and its application to fluid dynamics problems, 6th AIAA Theoretical Fluid Mechanics Conferencedoi:10.2514/6.2011-3112.

[26] S. Chaturantabut, D. Sorensen, Discrete empirical interpolation for nonlinear model reduction, Proceedings of the IEEE Conference on Decision and Control 32 (2010) 4316 – 4321. doi:10.1109/CDC.2009.5400045.

[27] S. An, T. Kim, D. James, Optimizing cubature for efficient integration of subspace deformations, ACM transactions on graphics 27 (2009) 165. doi:10.1145/1409060.1409118.

[28] C. Farhat, P. Avery, T. Chapman, J. Cortial, Dimensional reduction of nonlinear finite element dynamic models with finite rotations and energy-based mesh sampling and weighting for computational efficiency, International Journal for Numerical Methods in Engineering 98. doi:10.1002/nme.4668.

[29] J. Hernández, M. Caicedo-Silva, A. Ferrer Ferre, Dimensional hyper-reduction of nonlinear finite element models via empirical cubature, Computer Methods in Applied Mechanics and Engineering 313. doi:10.1016/j.cma.2016.10.022.

[30] F. Casenave, N. Akkari, F. Bordeu, C. Rey, D. Ryckelynck, A nonintrusive distributed reduced order modeling framework for nonlinear structural mechanics – application

to elastoviscoplastic computations, International Journal for Numerical Methods in Engineering 121. doi:10.1002/nme.6187.

[31] D. Ryckelynck, K. Lampoh, S. Quilicy, Hyper-reduced predictions for lifetime assessment of elasto-plastic structures, Meccanica 51. doi:10.1007/s11012-015-0244-7.

[32] D. Ryckelynck, Hyper-reduction of mechanical models involving internal variables, International Journal for Numerical Methods in Engineering 77 (2009) 75 – 89. doi:10.1002/nme.2406.

[33] P. Ciarlet, The finite element method for elliptic problems, Mathematics of Computation 36 (2002) xxviii+530. doi:10.2307/2007669.

[34] A. Carpinteri, F. Accornero, Multiple snap-back instabilities in progressive microcracking coalescence, Engineering Fracture Mechanics 187. doi:10.1016/j.engfracmech.2017.11.034.

[35] N. Vasios, Nonlinear analysis of structures : The arc length method: Formulation, implementation and applications.

[36] C. Eckart, G. Young, The approximation of one matrix by another of lower rank, Psychometrika 1 (1936) 211–218. doi:10.1007/BF02288367.

[37] R. Everson, L. Sirovich, Karhunen–loève procedure for gappy data, JOSA A 12. doi:10.1364/JOSAA.12.001657.

[38] L. Barriere, J.-C. Passieux, B. Castanié, S. Marguet, P. Cresta, An adaptive model reduction strategy for post-buckling analysis of stiffened structures, Thin-Walled Structures 73 (2013) 81–93. doi:10.1016/j.tws.2013.07.009.

[39] F. Pichi, G. Rozza, Reduced basis approaches for parametrized bifurcation problems held by non-linear von kármán equations, Journal of Scientific Computingdoi:10.1007/s10915-019-01003-3.

[40] S. H. Zhang, D. Zhao, C. Gao, Limit analysis of defect-free pipe elbow under internal pressure with mean yield criterion, Applied Mechanics and Materials 127. doi:10.4028/www.scientific.net/AMM.127.79.

[41] D. Ryckelynck, G. Laurent, S. Jules, Estimation of the validity domain of hyper-reduction approximations in generalized standard elastoviscoplasticity, Advanced Modeling and Simulation in Engineering Sciences 2. doi:10.1186/s40323-015-0027-7.

[42] M. d'Ocagne, Coordonnées parallèles et axiales, Gauthier-Villars.